PAPER

Check for updates

Enhanced visible-light photocatalytic performance of highly-dispersed Pt/g-C$_3$N$_4$ nanocomposites by one-step solvothermal treatment

Zhao Lu,[a] Wulin Song, *[ab] Chao Ouyang,[a] Hao Wang,[a] Dawen Zeng [a] and Changsheng Xie[a]

A highly dispersed Pt/g-C$_3$N$_4$ nanocomposite photocatalyst was successfully prepared by depositing platinum nanoparticles (NPs) onto the surface of g-C$_3$N$_4$ with uniform size. The nanocomposites were applied as an efficient visible-light-driven photocatalyst for the degradation of methyl orange (MO) and tetracycline hydrochloride (TC). The sample with a Pt loading amount of 2% exhibited the highest photocatalytic performance, about 7.82 (MO) and 4.30 (TC) times higher than that of the pure g-C$_3$N$_4$. The enhancement of the photocatalytic performance was attributed to the rapid separation of generated electron hole pairs resulting from the hybrid effect, which was confirmed by XPS spectra, photocurrent response experiment, electrochemical impedance spectroscopy measurements and photoluminescence spectra. As confirmed by X-ray photoelectron spectroscopy, there is a strong interaction between Pt NPs and g-C$_3$N$_4$; the delocalized pi bond in g-C$_3$N$_4$ with a high local electron density donates lone pair electrons to the empty d orbitals of Pt atoms. The combination between g-C$_3$N$_4$ and Pt promotes the separation of electron–hole pairs.

Introduction

Photocatalysis is expected to be a green technology for environmental remediation due to its effective utilization of solar energy. Several semiconductor photocatalysts have been widely studied, including TiO$_2$, ZnO, BiOX (Cl, Br, I), CdS and so on.[1–5] Recently, another promising 2D layered polymeric semiconductor, g-C$_3$N$_4$, has also gained comprehensive attention as a visible-light-driven photocatalyst.[6–8] Nevertheless, the photocatalytic performance of pure g-C$_3$N$_4$ is limited because of its weak absorption of visible light and charge recombination. Hence various approaches have been applied to modify its electronic structure and enhance its photocatalytic properties. For example, Han *et al.* prepared an atomically thin mesoporous nanomesh of graphitic carbon nitride to modify its structure.[9] Li *et al.* synthesized oxygen–g-C$_3$N$_4$ to induce intrinsic electronic and band structure modulation.[10] Jiang *et al.* constructed a p–n heterojunction photocatalyst by coupling nanostructured BiOI on the porous graphite-like C$_3$N$_4$, and the photocatalyst exhibited superior photocatalytic activity towards the degradation of MB which was attributed to the fast separation of electron–hole pairs.[11] Meanwhile, based on this mechanism, Jiang *et al.* also synthesized perovskite oxide ultrathin nanosheets/g-

C$_3$N$_4$ 2D-2D heterojunction photocatalysts, and the photocatalyst had excellent photocatalytic performance in the degradation of TC.[12] Zhu *et al.* prepared Ag/Fe$_3$O$_4$/g-C$_3$N$_4$ heterojunction photocatalyst to change the electron–hole separation processes.[13]

Particularly, combining g-C$_3$N$_4$ with different noble metals such as Ag, Au, Pd and Pt to form composites has been considered a feasible route. Li *et al.* constructed Ag/graphene-like g-C$_3$N$_4$ photocatalyst, and the composites displayed enhanced photocatalytic activity.[14] Olga Fontelles-Carceller *et al.* synthesized Ag/g-C$_3$N$_4$ composites and the catalysts exhibited enhanced photocatalysis performance towards toluene degradation.[15] F. Fina *et al.* reported that Pt–g-C$_3$N$_4$ with particles characterized by a high crystallinity results in a high H$_2$ evolution.[16] Xue *et al.* prepared Au/Pt/g-C$_3$N$_4$ and the composites showed enhanced photocatalytic activity for antibiotic degradation.[17] However, the interaction between noble metals and g-C$_3$N$_4$ was rarely concerned. As a matter of fact, the charge transfer is mainly finished through effective interfacial combination.[18–20]

Here, we presented a 0D–2D heterojunction photocatalyst by *in situ* growth of Pt NPs on g-C$_3$N$_4$ sheets with varied ratio. Meanwhile, the 2Pt/g-C$_3$N$_4$ exhibited a dramatically improved photocatalytic activity towards the degradation of MO and TC under visible light irradiation. Also, the possible mechanism was discussed and mainly attributed to the hybrid effect, there is a strong interaction between Pt NPs and g-C$_3$N$_4$, confirmed by XPS, the interaction between Pt NPs and g-C$_3$N$_4$ promotes efficient transfer of e$^-$ and high separation of electron–hole pairs.

^{a}State Key Laboratory of Materials Processing, Die & Mould Technology, Huazhong University of Science and Technology, 1037 Luoyu Road, Wuhan 430074, PR China
^{b}Analytical and Testing Center of Huazhong University of Science and Technology, Wuhan 430074, PR China

Experimental

Preparation of catalysts

g-C_3N_4 was synthesized by thermal polycondensation of urea. Typically, 10 g of urea was put into a ceramic crucible with a cover, heated at 550 °C for 4 h at a rising rate at 15 °C min^{-1} in a muffle furnace. After cooling to room temperature naturally, the resulting pale yellow products were collected and ground into powders. Pt/g-C_3N_4 was prepared through a simple water bath method. 0.2 g g-C_3N_4 was dispersed into 25 mL ethylene glycol (EG), then a certain amount of $H_2PtCl_6 \cdot 6H_2O$ and a solution of NaOH in EG were added to the g-C_3N_4 solution. Finally, a brown suspension was obtained by heating the mixed solution at 90 °C for 1 h under N_2 atmosphere. After cooling to room temperature naturally, the resulting product was centrifuged and washed with absolute ethanol and distilled water, followed by drying in a vacuum oven at 80 °C overnight. By varying the dosage of $H_2PtCl_6 \cdot 6H_2O$, a series of Pt/g-C_3N_4 nanocomposites were synthesized, labelled as xPt/g-C_3N_4, where x is the wt% (0.5, 1, 2 and 4) of Pt with respect to g-C_3N_4.

Characterization of catalysts

X-ray diffraction (XRD, X'Pert PRO diffractometer with Cu Kα radiation), high-resolution transmission electron microscopy (HRTEM, FEI Tecnai G2 F30 field-emission TEM), Fourier transform infrared (FT-IR) spectra were recorded from a KBr disk on the FT-IR Bruker Tensor27. X-ray photoelectron spectroscopy (XPS, VG Multilab2000 spectrometer) measurements were performed. UV-vis diffuse reflectance spectra (UV-vis DRS) was recorded at Shimadzu U-3010 spectrometer using $BaSO_4$ as a reference. The specific surface area and the pore size distribution were determined from N_2 adsorption–desorption isotherms at 77 K, obtained by a BRLSORP analyzer. The specific surface area was calculated from multipoint adsorption data within the linear segment of the N_2 adsorption isotherms, using Brunauer–Emmett–Teller theory. The pore size distribution was determined from the isotherms by using nonlocal density functional theory. Photoluminescence (PL) spectra was obtained on a Jasco FP-6500 with a laser excitation of 325 nm.

The photocurrent and electrochemical impedance spectroscopy measurements (EIS) were carried out on a Shanghai Chenhua CHI-660D electrochemical system by using a conventional three-electrode cell. The counter and the reference electrodes were platinum wire and saturated calomel electrode (SCE), respectively. The electrolyte solution was 0.1 M Na_2SO_4. The as-prepared photocatalyst powders were fixed to the film electrodes by the following method: firstly, 10 mg catalyst sample was mixed with 1 mL distilled water homogeneously (10 mg mL^{-1}). Then, the solution was spin-coated onto an ITO glass electrode. At last, the electrode was dried naturally for 12 h and then dried at 120 °C for 5 h.

Performance evolution of catalysts

The photocatalytic activities were evaluated by the degradation of MO (20 mg L^{-1}, 50 mL) and TC (20 mg L^{-1}, 100 mL) under visible light irradiation ($\lambda > 400$ nm), respectively. A 300 W Xe lamp (CEL-HXF300) with a 400 nm UV cut-off filter was applied light source, and a liquid trap system was used to keep the temperature steady. Generally, 50 mg catalyst was dispersed in the target solution. Prior to irradiation, the reaction suspensions were under vigorous stirring for 30 min to reach an absorption–desorption equilibrium. 5 mL solution was taken and centrifuged at every 5 minute intervals, and supernatant fluid was extracted immediately. The concentration was analysed by UV/vis spectroscopy. The degradation rate was calculated by C/C_0, where C was the concentration after irradiation, C_0 was the concentration of the reactant after adsorption–desorption equilibrium. A blank control test without photocatalyst was conducted for reference.

Results and discussion

XRD patterns

Fig. 1 shows the phase structures of the as-prepared samples. Two distinct diffraction peaks can be observed in the XRD patterns. The weak diffraction peak at 13.1° (100) and another strong diffraction peak at 27.5° (002) can be attributed to the in-plane structure of tri-s-triazine units and the graphitic layer stacking, severally.[21] After coupling with Pt NPs, there is no change in the peak positions of g-C_3N_4, indicating that Pt NPs are not incorporated into the lattice of g-C_3N_4. The characteristic peak at 39.7° (111) can be identified as Pt NPs in the 2Pt/g-C_3N_4 and 4Pt/g-C_3N_4.[22] Due to the low loading amount of Pt in 0.5Pt/g-C_3N_4 and 1Pt/g-C_3N_4, the peak is not distinct.

Morphologies

Fig. 2 displays the microstructures of g-C_3N_4 and 2Pt/g-C_3N_4. Fig. 2a is the TEM image of the pure g-C_3N_4, showing a layered structure with smooth surface. For the 2Pt/g-C_3N_4, the small-sized Pt NPs are evenly distributed on the surface of g-C_3N_4 as shown in Fig. 2b. HRTEM image shows clear lattice fringes of Pt NPs in Fig. 2c, and the lattice of 0.23 nm corresponds to the (111) planes of the Pt NPs, which is in accordance with the XRD result. Fig. 2d shows the Pt particle size distribution,
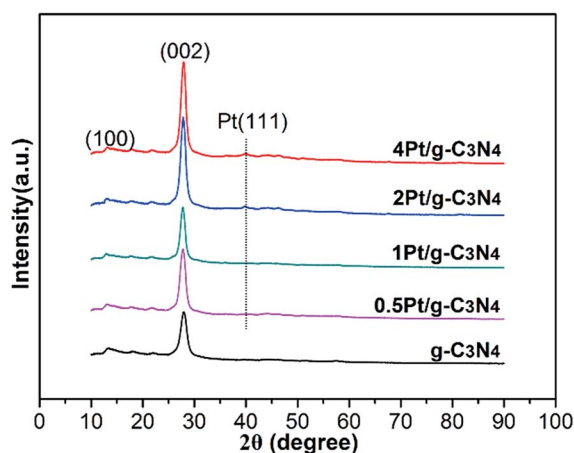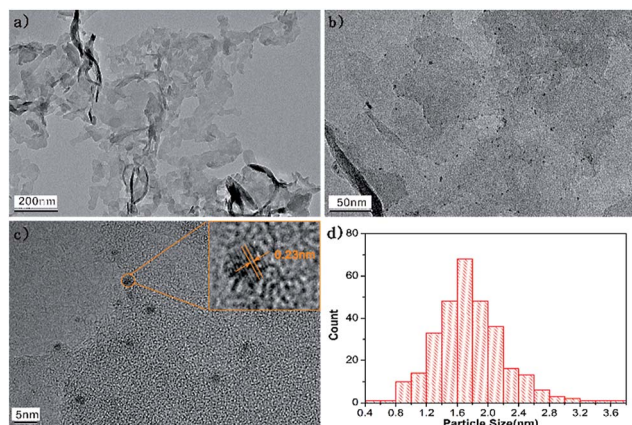

Fig. 1 XRD patterns of all samples.

Fig. 2 TEM images of g-C₃N₄ (a), 2Pt/g-C₃N₄ (b, c), and particle size distribution (d).

Fig. 4 XPS spectra: survey spectrum of 2Pt/C₃N₄.

demonstrating the particle size is rather uniform and the average size is 1.6 nm. Thus it can be seen that Pt NPs are well dispersed on the g-C₃N₄ successfully.

FT-IR spectroscopy analysis

Fig. 3 shows the local structures of all samples. For the pure g-C₃N₄, there are three characteristic bands: the absorption band at 1638 cm⁻¹ is attributed to C–N stretching vibration; the strong band at 1200–1600 cm⁻¹ is associated with the typical aromatic C–N stretching vibration; the band near 810 cm⁻¹ is related to characteristic bending vibration of tri-*s*-triazine ring units.[23–25] For all Pt/g-C₃N₄ samples, the FTIR spectra are similar to that of pure g-C₃N₄, indicating that the structure of g-C₃N₄ has no change. The results accord well with the result of XRD.

X-ray photoelectron spectroscopy

To study the chemical composition and interaction between Pt NPs and g-C₃N₄, XPS analysis was utilized, as shown in Fig. 4a. Fig. 4b shows the C 1s high resolution spectra, the peak at 288.4 eV can be distinguished for g-C₃N₄, which is assigned to
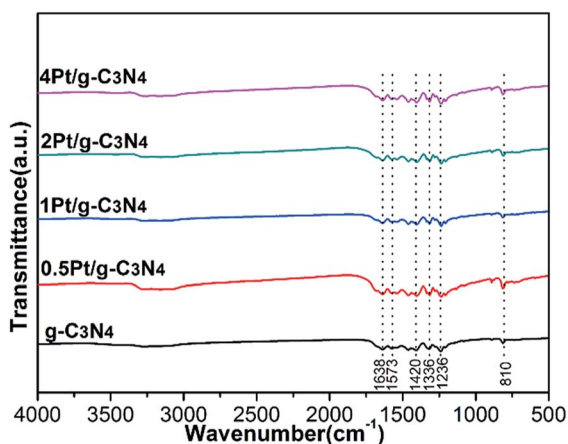
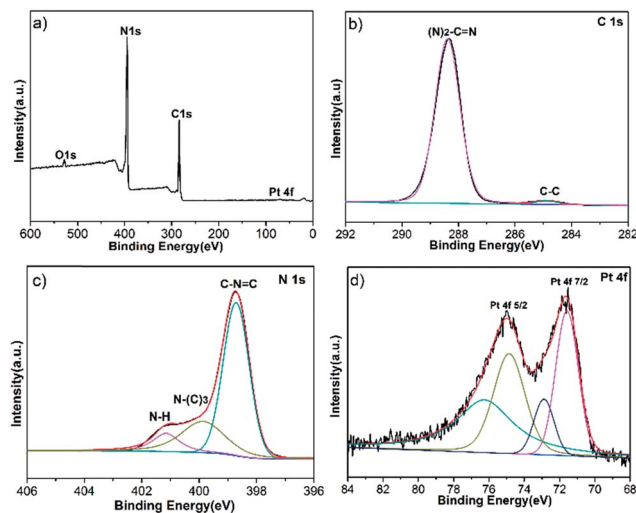sp₂-hybridized carbon in the unit of (N)₂–C=N. The peak shifts to a more positive position compared with pure g-C₃N₄ which is at 288.1 eV.[7] Meanwhile, the high resolution XPS spectra of N 1s region is shown in Fig. 4c, the binding energy of C=N–C bond (398.6 eV), N–(C)₃ (399.8 eV) and N–H (401.1 eV) all also increase in contrast with the pure g-C₃N₄.[7] Because the delocalized pi bond of g-C₃N₄ possesses high electron density, providing lone pairs electrons to d orbitals of Pt, leading to the decrease of electron density of g-C₃N₄. For the Pt 4f XPS spectra in Fig. 4d, two main peaks at 74.4 (Pt 4f₅/₂) and 70.9 eV (Pt 4f₇/₂) are indexed as metallic Pt⁰. Comparing with the standard Pt 4f₇/₂ binding energy of Pt⁰ (71.2 eV), the Pt 4f₇/₂ peak shifts to a more negative position, since the increase of electron density of Pt.[26] And another two weak peaks at 75.9 and 72.3 eV are assigned to Pt²⁺ chemical state, stemming from incomplete reduction of Pt⁴⁺.[27] Thus g-C₃N₄ coupling with Pt NPs promotes the separation of electron–hole pairs.

UV-vis diffuse reflection spectra

Fig. 5 shows the UV-vis diffuse reflectance absorption spectra of all samples. Pure g-C₃N₄ exhibits an absorption edge at about 450 nm. After coupling with Pt NPs, the absorption edge has no change, indicating that introduction of Pt NPs does not affect the band structure. Moreover, background absorption in the visible light region enhances with increasing Pt content due to localized surface plasmon resonance.[28] This result indicates that the Pt is only supported on the surface of g-C₃N₄ and not incorporated into the lattice of g-C₃N₄, which is consistent with the XRD and XPS results.

BET surface areas and pore structure

The BET surface areas and the pore size distributions of all samples are also measured, as shown in Fig. 6 and Table 1. The specific surface area of the pure g-C₃N₄ is 93.5 m² g⁻¹. After coupling with Pt NPs, the specific surface area of Pt/g-C₃N₄ increases, and the specific surface area increased slowing with
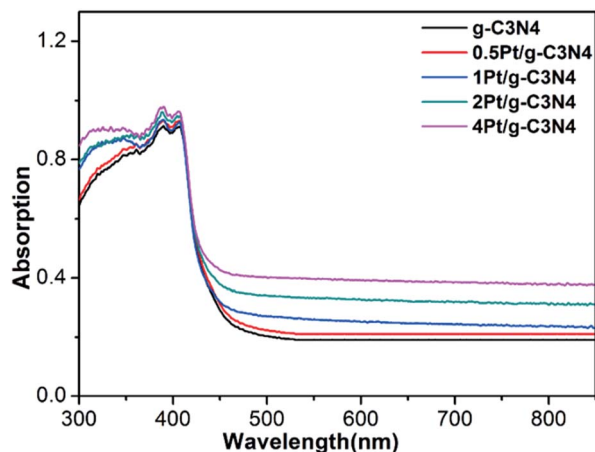

Fig. 3 FT-IR patterns of all samples.
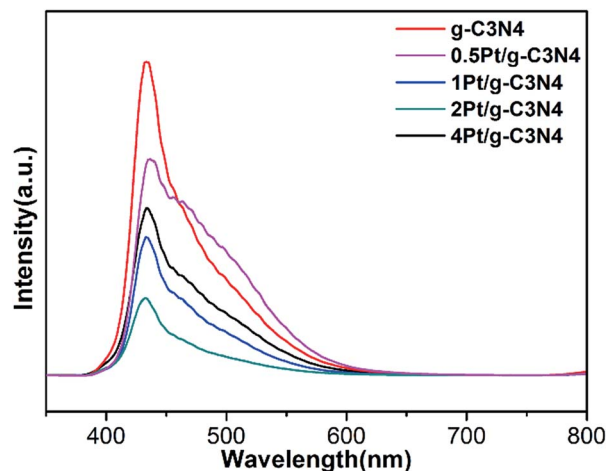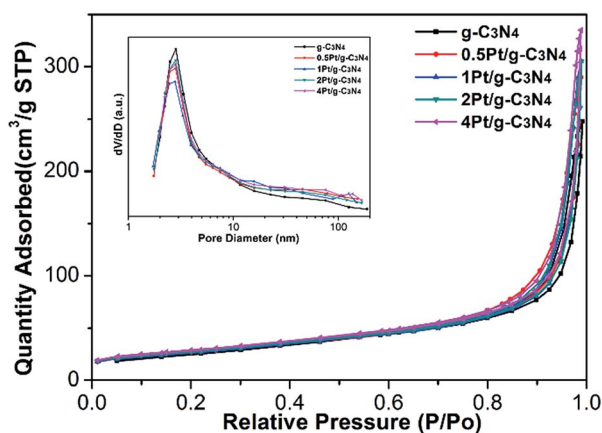
Fig. 5 UV-vis diffuse reflectance absorption spectra of all samples.

Fig. 6 N_2 adsorption–desorption isotherms of all samples, and the corresponding normalized pore-size distribution (inset).

Table 1 The S_{BET} and peak pore size of all samples

Sample name	S_{BET} (m^2 g^{-1})	Peak pore size (nm)
g-C$_3$N$_4$	93.5	2.8
0.5Pt/g-C$_3$N$_4$	94.4	2.8
1Pt/g-C$_3$N$_4$	94.8	2.8
2Pt/g-C$_3$N$_4$	96.9	2.8
4Pt/g-C$_3$N$_4$	100.7	2.8

the increasing amount of Pt NPs, which is owning to the infinitesimal particle size of Pt NPs. Moreover, according to the Barret–Joyner–Halenda (BJH) pore size distributions of all samples, all of them own the similar small mesoporous at 2.8 nm, indicating that the microstructures have no change after coupling with Pt NPs.

PL measurements

Fig. 7 shows the PL spectra of all samples. The PL emission intensity of the pure g-C$_3$N$_4$ sample is highest, indicating that

Fig. 7 PL spectra of all samples.

the recombination of electron–hole pairs is the most serious. Obviously, after coupling with Pt NPs, the PL intensity steps down, indicating the promotion in the electron–hole pairs separation. However, the PL intensity of 4Pt/g-C$_3$N$_4$ increases compared with 2Pt/g-C$_3$N$_4$, since the overloaded Pt NPs become recombination center.[28] So the content of Pt plays a significant influence on the activity.

Photoelectrochemical measurements

To further investigate the excitation and transfer of photo-generated charge carriers of 2Pt/g-C$_3$N$_4$, the photocurrent response (J–t) experiments and EIS Nyquist analysis were performed via several on–off cycles under visible light irradiation. The photocurrent is shown in Fig. 8a; it is obvious that the photocurrent of g-C$_3$N$_4$ display good reproducibility and stability under several on–off cycles of intermittent irradiation. Furthermore, the transient photocurrent density of 2Pt/g-C$_3$N$_4$ is obviously higher than that of g-C$_3$N$_4$ severally, indicating that the Schottky junctions formed between Pt NPs and g-C$_3$N$_4$ and coupling with Pt NPs could significantly improve the separation efficiency of photogenerated charge carriers. EIS Nyquist analysis is shown in Fig. 8b, the radius of each arc is related to the charge transfer process at the electrode/electrolyte interface, the smaller the radius of each arc, the better the separation of electron–hole pairs.[29,30] So 2Pt/g-C$_3$N$_4$ has a more effective separation of photogenerated electron–hole pairs and faster
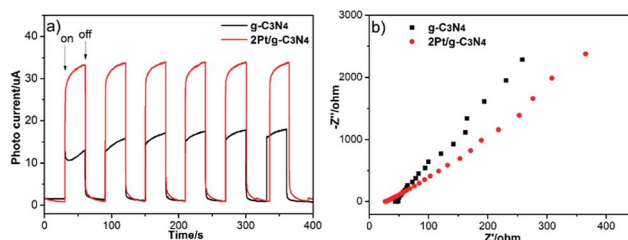

Fig. 8 Transient photocurrent responses (a) and electrochemical impedance spectroscopy (b).

interfacial electron transfer. The result also indicates that coupling with Pt NPs is benefit to electron transfer, which agrees well with the result of the transient photocurrent responses.

Photocatalytic activity

Fig. 9a displays the photocatalytic properties of all samples based on the degradation of MO under visible light irradiation, the results indicate that all Pt/g-C_3N_4 samples exhibit better catalytic activity than g-C_3N_4. When the mass ratio of Pt/g-C_3N_4 is 2 (2Pt/g-C_3N_4), the photocatalytic activity is best and the MO is degraded nearly completely after 40 min reaction, whereas only 40.2% of MO could be decomposed for the pure g-C_3N_4. The photocatalysis degradation follows the first-order kinetics. The kinetics could be expressed as follows: $-\ln(C/C_0) = k_{app}t$. Fig. 9b presents the linear relationship between $\ln(C/C_0)$ and time, where C/C_0 is the normalized as MO concentration, t is the reaction time, and k is the reaction rate constant. The corresponded apparent pseudo-first-order rate constant k_{app} of 2Pt/g-C_3N_4 was 0.09282 min^{-1}, which is about 7.82 times higher than that of g-C_3N_4.

TC is chosen as another different type of model pollutant to evaluate the photocatalytic activity as shown in Fig. 9c. The results indicate that the 2Pt/g-C_3N_4 exhibits excellent photocatalytic activity for the photodegradation of TC and TC removal reaches about 84.1% after 40 min reaction, but g-C_3N_4 exhibits a poorer photocatalytic activity and the photodegradation rate of MO only reaches about 39.9%. Fig. 9d presents the linear relationship between $\ln(C/C_0)$ and time toward the degradation of TC. The photocatalytic decomposition rate of 2Pt/g-C_3N_4 is 0.04819 min^{-1}, which is about 4.30 times of over g-C_3N_4.

Besides the photocatalytic performance, the stability of a catalyst is also one key point for its practical applications, so the recycling experiments were conducted on the 2Pt/g-C_3N_4 sample under same conditions. According to the results shown in Fig. 10, whether for photodegradation of MO or TC, the
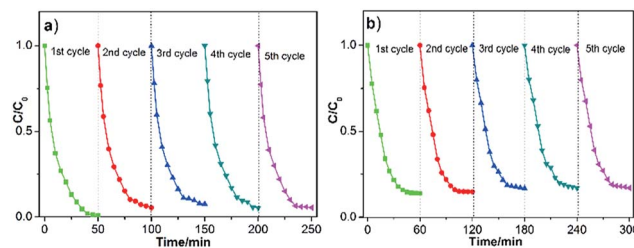

Fig. 10 The stability study for the photocatalytic MO (a) and TC (b) degradation by 2Pt/g-C_3N_4.
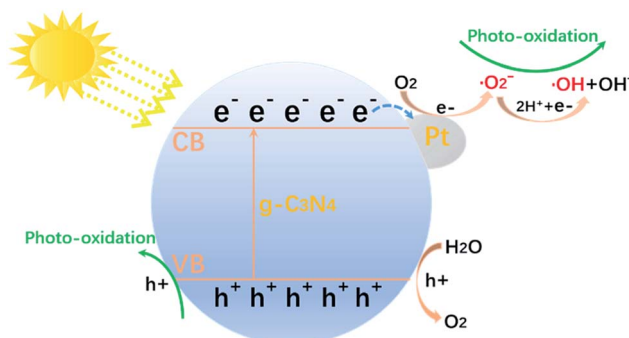

Fig. 11 Schematic illustrations of photocatalytic process.

sample still exhibits superior activity after five cycles, suggesting the excellent stability of the 2Pt/g-C_3N_4 sample during the photocatalytic reaction.

Mechanism discussion

Compared to the pure g-C_3N_4, the photocatalytic performance of all Pt/g-C_3N_4 were improved. Based on the above analysis, when the Pt/g-C_3N_4 nanocomposites is irradiated by visible light, electrons of g-C_3N_4 are excited from the valence band to the conduction band, leaving holes in the valence band. This moment Pt NPs act as electron acceptors, the excited electrons transfer from valence band of g-C_3N_4 to Pt NPs. So decoration with Pt NPs could promote the separation of electron–hole pairs. This separation process is shown in Fig. 11. However, the reaction rate constant firstly increased and then decreased with the Pt mass rising. With the content of Pt increasing from 0 to 2 wt%, the contact area of g-C_3N_4 and Pt NPs increased, leading to the promotion in efficient transfer of e^- and separation of electron–hole pairs. Nevertheless, the overmuch amount of Pt NPs would result in an increase in the Schottky barrier height and an enhanced rate of electron–hole recombination.[31,32]

Conclusions

In conclusion, we have prepared highly dispersed Pt/g-C_3N_4 composites through a reduction process in the EG solvent. These hybrids exhibit significantly enhanced photocatalytic activities towards the degradation of MO and TC compared to pure g-C_3N_4. This is attributed to the faster separation of photogenerated electron–hole pairs. The content of Pt displays
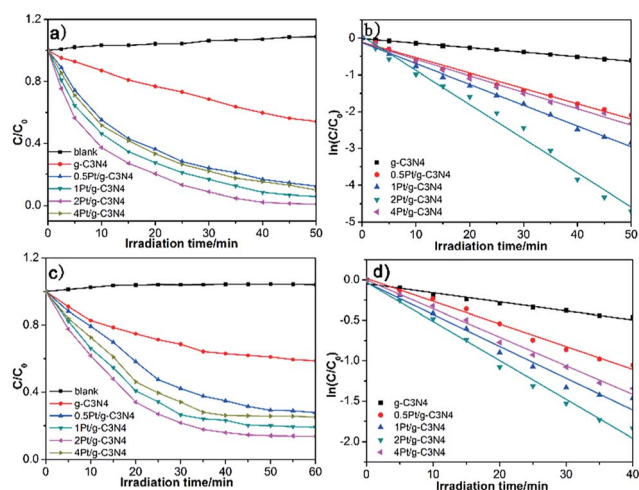

Fig. 9 Photodegradation rate of MO (a) and TC (c) under visible light irradiation; corresponding kinetic curves of MO (b) and TC (d) for all samples.

a significant influence on the activities, the content of Pt from 0 to 2 wt%, the activities improve because Pt NPs act as electron acceptor and promote the separation of electron–hole pairs. However, the content of Pt increases continuously, the activities decrease, since Pt becomes the recombination centre of electron–hole pairs. This indicates that the nanocomposites material with highly efficient visible photocatalytic activities has been provided.

Acknowledgements

References

1 X. Chen, L. Liu, P. Y. Yu and S. S. Mao, *Science*, 2011, **331**, 746–750.

2 J. Wang, Z. Wang, B. Huang, Y. Ma, Y. Liu, X. Qin, X. Zhang and Y. Dai, *ACS Appl. Mater. Interfaces*, 2012, **4**, 4024–4030.

3 J. Jiang, K. Zhao, X. Xiao and L. Zhang, *J. Am. Chem. Soc.*, 2012, **134**, 4473–4476.

4 D. Zhang, J. Li, Q. Wang and Q. Wu, *J. Mater. Chem. A*, 2013, **1**, 8622.

5 Q. Li, B. Guo, J. Yu, J. Ran, B. Zhang, H. Yan and J. R. Gong, *J. Am. Chem. Soc.*, 2011, **133**, 10878–10884.

6 H. Wang, X. Zhang, J. Xie, J. Zhang, P. Ma, B. Pan and Y. Xie, *Nanoscale*, 2015, **7**, 5152–5156.

7 Z. Lu, L. Zeng, W. Song, Z. Qin, D. Zeng and C. Xie, *Appl. Catal., B*, 2017, **202**, 489–499.

8 H. Zhao, H. Yu, X. Quan, S. Chen, H. Zhao and H. Wang, *RSC Adv.*, 2014, **4**, 624–628.

9 Q. Han, B. Wang, J. Gao, Z. Cheng, Y. Zhao, Z. Zhang and L. Qu, *ACS Nano*, 2016, **10**, 2745–2751.

10 J. Li, B. Shen, Z. Hong, B. Lin, B. Gao and Y. Chen, *Chem. Commun.*, 2012, **48**, 12017–12019.

11 D. Jiang, L. Chen, J. Zhu, M. Chen, W. Shi and J. Xie, *Dalton Trans.*, 2013, **42**, 15726–15734.

12 D. Jiang, T. Wang, Q. Xu, D. Li, S. Meng and M. Chen, *Appl. Catal., B*, 2017, **201**, 617–628.

13 Z. Zhu, Z. Lu, D. Wang, X. Tang, Y. Yan, W. Shi, Y. Wang, N. Gao, X. Yao and H. Dong, *Appl. Catal., B*, 2016, **118**, 115–122.

14 H. Li, Y. Jing, X. Ma, T. Liu, L. Yang, B. Liu, S. Yin, Y. Wei and Y. Wang, *RSC Adv.*, 2017, **7**, 8688–8693.

15 O. Fontelles-Carceller, M. J. Munoz-Batista, M. Fernandez-Garcia and A. Kubacka, *ACS Appl. Mater. Interfaceser*, 2016, **8**, 2617–2627.

16 F. Fina, H. Menard and J. T. Irvine, *Phys. Chem. Chem. Phys.*, 2015, **17**, 13929–13936.

17 J. Xue, S. Ma, Y. Zhou, Z. Zhang and M. He, *ACS Appl. Mater. Interfaces*, 2015, **7**, 9630–9637.

18 Q. Huang, S. Tian, D. Zeng, X. Wang, W. Song, Y. Li, W. Xiao and C. Xie, *ACS Catal.*, 2013, **3**, 1477–1485.

19 Z. Zhang, J. Huang, M. Zhang, Q. Yuan and B. Dong, *Appl. Catal., B*, 2015, 298–305, DOI: 10.1016/j.apcatb.2014.08.013.

20 D. Jiang, J. Li, C. Xing, Z. Zhang, S. Meng and M. Chen, *ACS Appl. Mater. Interfaces*, 2015, **7**, 19234–19242.

21 Q. Lin, L. Li, S. Liang, M. Liu, J. Bi and L. Wu, *Appl. Catal., B*, 2015, **163**, 135–142.

22 B. Y. Xia, B. Wang, H. B. Wu, Z. Liu, X. Wang and X. W. Lou, *J. Mater. Chem.*, 2012, **22**, 16499.

23 J. Di, J. Xia, S. Yin, H. Xu, M. He, H. Li, L. Xu and Y. Jiang, *RSC Adv.*, 2013, **3**, 19624.

24 Y. Bai, P.-Q. Wang, J.-Y. Liu and X.-J. Liu, *RSC Adv.*, 2014, **4**, 19456.

25 Y. He, L. Zhang, X. Wang, Y. Wu, H. Lin, L. Zhao, W. Weng, H. Wan and M. Fan, *RSC Adv.*, 2014, **4**, 13610.

26 S. Cao, J. Jiang, B. Zhu and J. Yu, *Phys. Chem. Chem. Phys.*, 2016, **18**, 19457–19463.

27 J. Yu, K. Wang, W. Xiao and B. Cheng, *Phys. Chem. Chem. Phys.*, 2014, **16**, 11492–11501.

28 W. J. Ong, L. L. Tan, S. P. Chai and S. T. Yong, *Dalton Trans.*, 2015, **44**, 1249–1257.

29 C. Ye, J.-X. Li, Z.-J. Li, X.-B. Li, X.-B. Fan, L.-P. Zhang, B. Chen, C.-H. Tung and L.-Z. Wu, *ACS Catal.*, 2015, **5**, 6973–6979.

30 Q. Xu, C. Jiang, B. Cheng and J. Yu, *Dalton Trans.*, 2017, DOI: 10.1039/c7dt00629b.

31 S. Ma, S. Zhan, Y. Jia, Q. Shi and Q. Zhou, *Appl. Catal., B*, 2016, **186**, 77–87.

32 K. Li, Z. Zeng, L. Yan, S. Luo, X. Luo, M. Huo and Y. Guo, *Appl. Catal., B*, 2015, **165**, 428–437.